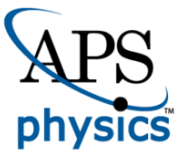

Actuation of Janus Emulsion Droplets via Optothermally Induced Marangoni Forces

Sara Nagelberg, Jan F. Totz, Matthäus Mittasch, Vishnu Sresht, Lukas Zeininger, Timothy M. Swager, Moritz Kreysing, and Mathias Kolle

Phys. Rev. Lett. **127**, 144503 — Published 29 September 2021

DOI: 10.1103/PhysRevLett.127.144503

Actuation of Janus Emulsion Droplets via Optothermally Induced Marangoni Forces

Sara Nagelberg,[1,*] Jan F. Totz,[1,2,*] Matthäus Mittasch,[3] Vishnu Sresht,[4] Lukas Zeininger,[5,6] Timothy M. Swager,[5] Moritz Kreysing,[3,7] and Mathias Kolle[1,†]

[1] *Department of Mechanical Engineering, Massachusetts Institute of Technology, Cambridge, USA*
[2] *Department of Mathematics, Massachusetts Institute of Technology, Cambridge, USA*
[3] *Max Planck Institute of Molecular Cell Biology and Genetics, Dresden, Germany*
[4] *Department of Chemical Engineering, Massachusetts Institute of Technology, Cambridge, USA*
[5] *Department of Chemistry, Massachusetts Institute of Technology, Cambridge, USA*
[6] *Max Planck Institute of Colloids & Interfaces, Potsdam, Germany*
[7] *Center for Systems Biology Dresden & Physics of Life, Cluster of Excellence, Technical University Dresden, Germany*

Micro-scale Janus emulsions represent a versatile material platform for dynamic refractive, reflective, and light-emitting optical components. Here, we present a mechanism for droplet actuation that exploits thermocapillarity. Using optically induced thermal gradients, an interfacial tension differential is generated across the surfactant-free internal capillary interface of Janus droplets. The interfacial tension differential causes droplet-internal Marangoni flows and a net torque, resulting in a predictable and controllable reorientation of the droplets. The effect can be quantitatively described with a simple model that balances gravitational and thermal torques. Occurring in small thermal gradients, these optothermally-induced Marangoni dynamics represent a promising mechanism for controlling droplet-based micro-optical components.

Many micro-fluidic technologies, including droplet-based sorting and sensing, chemical micro-reactors, and tunable fluidic micro-optics, are enabled by the precise manipulation of micro-scale droplets [1–3]. Complex droplet morphologies, such as liquid Janus particles [4] and multi-phase emulsions [5, 6], are relevant in a variety of applications, including drug delivery [7, 8], optics [9–11], biochemical sensors [12–15], and cosmetics [16]. Many of these applications rely on the ability to configure and optimize the droplet morphology. Since emulsion morphologies are usually stabilized with several surfactants, their configuration can be controlled by tuning the surfactant concentrations in the droplet medium or by dynamically modifying the surfactants' strength, for instance through optical stimulation [5, 9]. These control mechanisms require careful tuning of the chemical environment and the design of sophisticated stimuli-responsive surfactants.

Here, we present a simple alternative for controlling emulsion droplet configuration that does not require chemical modification of the surrounding medium. The orientation of bi-phase emulsion droplets, formed from immiscible hydrocarbons and fluorocarbons, can be manipulated physically with a small temperature gradient generated with a focused near-infrared laser in the fluid medium (Fig. 1a). Droplets are observed to pan (see schematic in Fig. 1b, c) and tilt (Fig. 1d,e) as they respond to the presence and movement of the laser spot. The thermal gradient generated by the laser induces an interfacial tension gradient along the droplets' internal surfactant-free interface (Fig. 1e). This interfacial tension gradient gives rise to Marangoni flows inside the droplets and a net torque, leading to droplet re-orientation. The tilt angle of the bi-phase emulsion droplets is determined by the balance of gravitational torque, which occurs due to the different densities of the constituent phases, and the torque associated with the opto-thermal Marangoni effects (Fig. 1e).

Thermal gradients are known to cause gradients in interfacial tension along a fluid-fluid interface [17–19]. Such gradients result in a net stress along the fluid interface causing Marangoni flows. Marangoni effects can also originate from chemical gradients, as observed in the famous tears of wine [20], and can cause emulsion droplets to act as self propelling micro-swimmers, driven by spontaneous symmetry-breaking or optically stimulated surfactant reconfiguration [21–24]. The associated behavior of a single-phase droplet or bubble in a temperature gradient is well understood [25] and photothermal control of single phase droplets has been demonstrated in a number of microfluidic systems [26–30]. Theoretical studies of thermo-capillary flows in a partially engulfed multi-phase droplet show that the translation velocity of a droplet depends sensitively on its morphology and the viscosity of its constituent phases [31, 32]. In experiments, the situation is further complicated due to the presence of surfactants, which are necessary for stabilizing emulsion [33], and controlling the droplets' morphology [5]. When subjected to a rise in temperature, surfactants may cause an increase in interfacial tension due to enhanced chemical cohesion [27], acting in opposition to conventional thermal Marangoni forces. The redistribution of surfactants on the surface will also act to mitigate any thermally-induced interfacial tension gradients [34, 35].

In our experiments, these various competing effects suppress interfacial tension gradients in the outer surfaces of the bi-phase emulsion droplets, when a thermal gradient is applied. The observed Marangoni flows and

* these authors contributed equally to this work
† mkolle@mit.edu

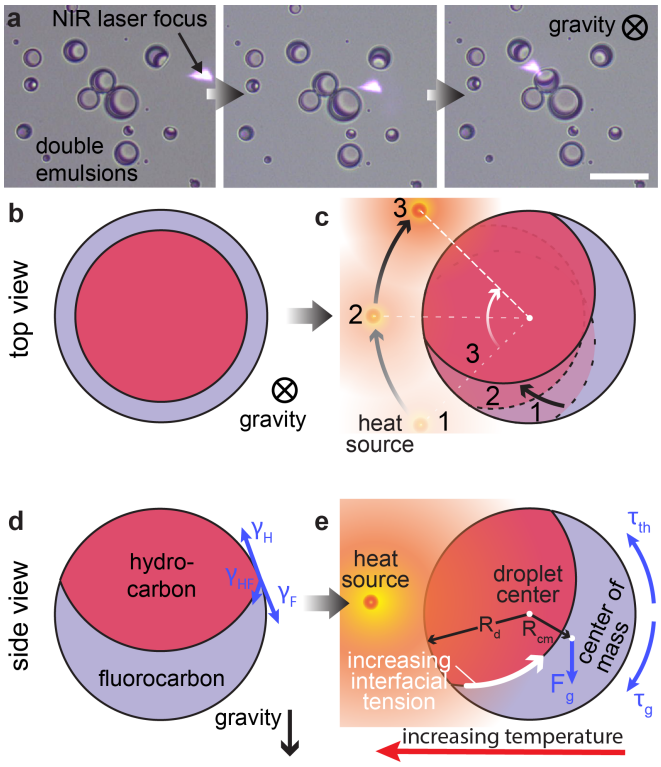

FIG. 1. **Emulsion droplets re-orient toward a laser spot, which acts as a localized heat source. a)** Emulsion droplets formed from heptane and perfluorohexane rotate toward the heat source; scale bar 50 µm (Supplementary video V1). **b**, **c)** Top-view schematics of an emulsion droplet formed from a lighter hydrocarbon (pink) and a heavier fluorocarbon (grey) when aligned solely by gravity (b) and when a thermal source is passing by (c). **d)** Side-view schematic of the same droplet, showing the relevant interfacial tensions γ_H, γ_F, and γ_{FH}. **e)** The droplet's response in a thermal field, which creates an interfacial tension gradient at the droplet-internal capillary surface and results in a steady-state tilt with thermally-induced torque τ_{th} and gravitational torque τ_g being balanced. R_d - droplet radius, R_{cm} - distance between center of rotation and center of mass, F_g - gravitational force.

the associated reorientation of the droplets is therefore primarily driven by the surfactant-free capillary interface between the two phases. This is readily apparent when comparing the clearly observable flows in and around a Janus droplet exposed to a thermal gradient (Fig.2) with the absence of directional flows around single-phase droplets made from the emulsion's constituent phases (Supplementary Fig. S1). We visualize thermally induced Marangoni flows around the emulsion droplets by dispersing fluorescent particles in the surrounding aqueous medium (Supplementary video V2) and map the flow fields using particle imaging velocimetry [36]. When subjected to a laser-induced thermal gradient, substantial fluid motion can be perceived in the vicinity of bi-phase droplets (Fig. 2a, c). The presence of a small amount of phase impurities inside some droplets allowed us to qualitatively map the flow fields in the fluorocarbon phase (Fig. 2e). The experimentally observed flow patterns are closely matched by the theoretical flow fields obtained through finite element modeling (Fig. 2b, d, f), with experimentally estimated fluid velocities on internal interface and droplet surface assigned as a Dirichlet condition (Supplementary section II.C). Further, with the approximated flow field at the droplet interface, we find that the net force acting on the droplet vanishes, $\vec{F} = \vec{0}$ (Supplementary section II.C) [37]. Single-phase droplets composed of either emulsion phase exhibit no systematic external flow (Supplementary Fig. S1), which indicates that the exterior droplet interfaces do not play a role in the observed dynamics. The internal interface between

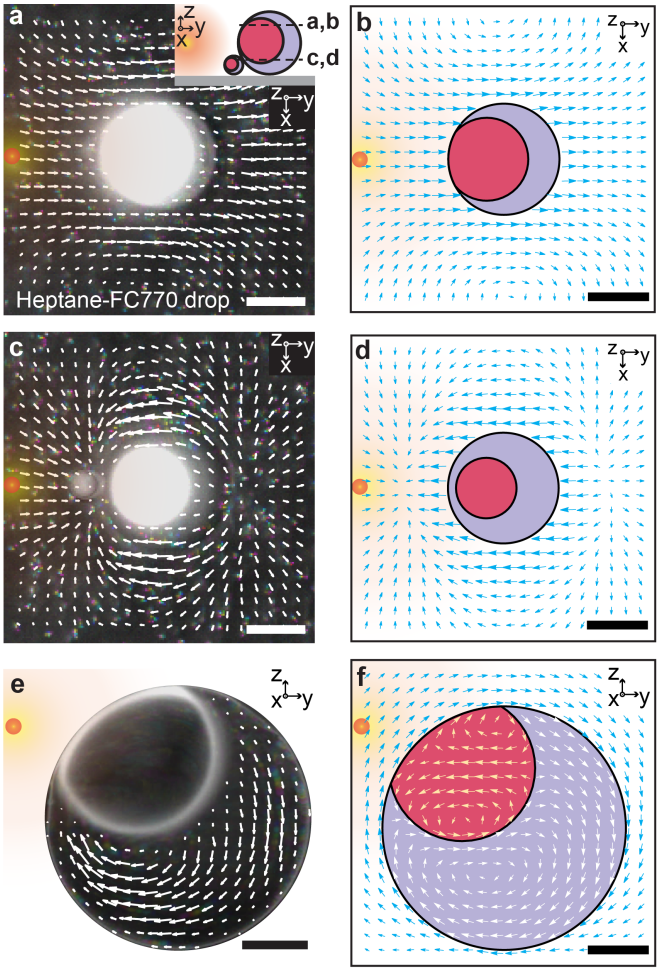

FIG. 2. **Particle imaging velocimetry data and finite element modeling reveal thermocapillary flows around and in bi-phase droplets. a, c)** The exterior flows visualized in top view around individual heptane–FC-770 droplets at different height levels match the fields that are obtained by **b, d)** finite element modeling in the same planes. The inset in (a) locates the optical slices shown in (a-d). The location of the IR laser spot is marked schematically with orange dots. **e)** Interior flow fields seen in the FC-770 phase of an 80 µm-sized droplet match **f)** modeled flow fields. All scale bars are 20 µm.

the two constituent phases is the critical driver for the manifestation of the observed dynamics.

To assess how the curvature of the internal capillary surface and the magnitude of the thermal differential affect the droplet dynamics, we systematically varied the distance between the laser spot and droplets with different morphologies and quantified their steady-state tilt angle α^* (Fig. 3). To modify the droplet morphology, we adjust the interfacial tensions between the constituent oils and the aqueous medium by changing the relative surfactant concentrations [5]. Droplets with a large internal interface curvature tilt significantly more than similarly-sized droplets with smaller interface curvature (Fig. 3a-c). For all tested droplet configurations, the steady-state rotation angle α^* decreased with increasing distance between droplet and heat source (Fig. 3d).

For our experiments, we used Fluorinert FC-770 and heptane to form approximately spherical bi-phase emulsions. FC-770 has a significantly higher density ($\rho_F = 1793\,\mathrm{kg\,m^{-3}}$) than heptane ($\rho_H = 684\,\mathrm{kg\,m^{-3}}$), resulting in a pronounced torque, when the droplets' symmetry axis is not aligned with gravity. The rotation of bi-phase droplets in a thermal gradient is opposed by this gravitational torque. As the droplets reach the steady-state rotation angle α^* the thermally induced torque is balanced by the gravitational torque. The gravitational torque can be mathematically expressed as $\tau_g = R_{\mathrm{cm}} \cdot Mg \sin\alpha^*$, where M is the total mass of the droplet, $g = 9.81\,\mathrm{m\,s^{-2}}$ is the gravitational constant, and R_{cm} is the distance from the droplet's center of rotation to its center of mass (Fig. 1e; details in Supplementary section II.A). This allowed us to quantify the magnitude of the thermally induced torque as a function of droplet morphology and distance between droplets and heat source (Fig. 3e).

The observed dependence of the droplet rotation on the thermal differential and internal interface curvature can be captured in a simple theoretical model: to determine the optically-induced thermal torque and steady-state rotation angle α^* for a given droplet geometry, we minimize the sum of gravitational energy $E_g(\alpha)$ and the energy $E_{\mathrm{th}}(\alpha)$ resulting from the thermally induced variation in interfacial tension across the droplet-internal capillary interface with respect to the droplet's tilt angle α (detailed discussion in Supplementary section II.B) [38–40]. This approach is equivalent to balancing gravitational torque $\tau_{\mathrm{g}}(\alpha)$ and thermally induced torque $\tau_{\mathrm{th}}(\alpha)$. The two energies can be expressed as

$$E_{\mathrm{g}}(\alpha) = R_{\mathrm{cm}}\, Mg\,(1-\cos\alpha) \tag{1}$$

$$E_{\mathrm{th}}(\alpha) = \int_{\Omega_{\mathrm{i}}} \gamma_{\mathrm{FH}}\left(T(\vec{r},\alpha)\right)\, dA\,. \tag{2}$$

The shape of the curved capillary interface Ω_{i} between the droplet's constituent phases can be described as a spherical cap with surface area $A_{\mathrm{i}} = 2\pi R_{\mathrm{i}}^2(1-\cos\theta_{\mathrm{i}})$, where R_{i} is the radius of curvature of the internal interface and θ_{i} represents the spherical cap's apex half angle (Fig. S4). To allow for an analytical solution, we linearize the surface tension dependence on temperature $\gamma_{\mathrm{FH}}(T) = \gamma_0 + \gamma_1 T$ and approximate the spatial temperature profile in a co-rotating droplet reference frame as $T(\vec{r},\alpha) = T_0 + \vec{r}\cdot\vec{n}(\alpha)\frac{\Delta T}{2R_{\mathrm{d}}}$. Here, R_{d} is the droplet radius, $\vec{r}$ the position vector measured from the droplet center, $\vec{n}(\alpha)$ the direction of the thermal gradient in the co-rotating reference frame, and ΔT the temperature differential across the droplet. The steady state rotation angle α^* can then be expressed analytically as

$$\tan\alpha^* = \frac{\gamma_1 \frac{\Delta T}{2R_{\mathrm{d}}} A_{\mathrm{i}} \left(d - \frac{1}{2}R_{\mathrm{i}}(1+\cos\theta_{\mathrm{i}})\right)}{R_{\mathrm{cm}}\, Mg}\,, \tag{3}$$

where d is a morphological parameter that describes the distance between the droplet center and the center of curvature of the internal interface (derivations in Supplementary sections II.A, B).

By applying this simple model to the experimentally studied droplet morphologies shown in Fig. 3, we recover the observed behavior qualitatively. The droplets all exhibit a very similar gravitational energy dependence on the rotation angle α (Fig. 4a), since their mass and center of gravity are very similar. However, they show an order of magnitude difference in their surface energies due to their different capillary interface curvatures (Fig. 4b).

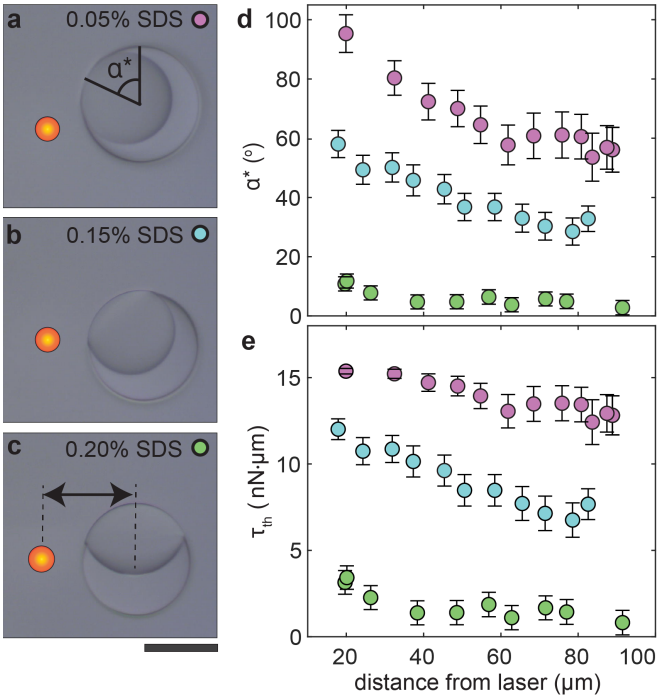

FIG. 3. **Quantifying rotation in thermal gradients for different droplet morphologies. a-c)** Side view images of droplets in the vicinity of a focused NIR laser in 0.4 wt% Zonyl and varying sodium dodecyl sulfate (SDS) concentrations to vary interface curvature - 0.05 wt% SDS (a, magenta), 0.15 wt% SDS (b, cyan), 0.20 wt% SDS (c, green); scale bar 50 µm. **d)** Steady-state rotation angle α^* of droplets in (a-c) and **e)** the corresponding thermal torque τ_{th} vs. distance from the laser spot. Morphological droplet parameters are listed in the Supplementary (table S2).

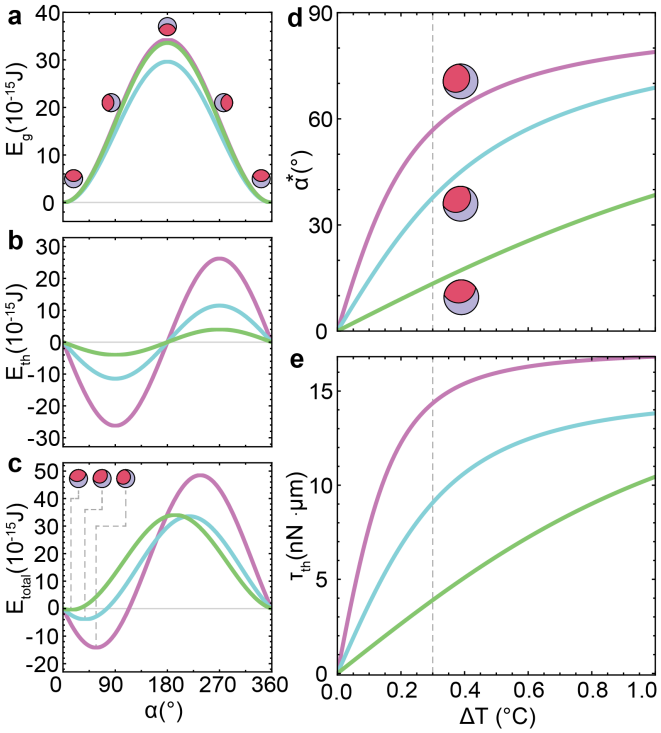

FIG. 4. **Modeling of droplet response: energy balance, resulting rotation angles, and torques. a-c)** Potential energy E_g due to gravity, energy E_γ due to thermally induced surface tension gradient, and the sum of both vs. rotation angle α. **d, e)** Steady state rotation angle α^* and thermal torque τ_{th} vs. temperature differential ΔT across droplet. The three differently shaded curves represent droplet geometries with increasing internal interface curvature that match the experimentally observed geometries shown in Fig. 3; $R_i = 0.82R_d$ (magenta), $R_i = 0.86R_d$ (cyan), $R_i = 0.99R_d$ (green), $\gamma_1 = -0.2\,\mathrm{mN\,m^{-1}\,K^{-1}}$.

This shifts the global minimum in the rotational energy landscape away from 0° towards larger tilts (Fig. 4c). In agreement with experiments (where the temperature differential decreases with distance from the laser spot), the orientation angle grows monotonically with increasing temperature differentials for all shown morphologies until it saturates at 90° (Fig. 4d). Correspondingly, the thermal torque grows as well (Fig. 4e).

The droplets' dynamic response to thermal gradients is observable at a laser power of $\sim 50\,\mathrm{mW}$ without any absorption-enhancing dye in the aqueous medium. In addition, we observe small translational motion, if droplets are exposed to significantly higher laser power ($\sim 150\,\mathrm{mW}$, see video V3 and Fig. S3), which suggests that the thermal differentials required to induce droplet rotation are significantly smaller than the temperature gradients needed for single-phase droplet manipulation [27, 28].

To estimate the magnitude of the thermal gradient needed to induce droplet reorientation, we harnessed the temperature-dependent fluorescence of 2' 7'-dichlorofluorescein (FL27) [41, 42]. Unlike other common organic dyes, whose fluorescence decreases with increasing temperature [43], FL27 exhibits increased light emission in the Anti-Stokes band for higher temperatures (when excited with green light of 532 nm wavelength). This positive correlation of temperature and Anti-Stokes emission can clearly be seen (Fig. 5a), when collecting the emitted light with a short-pass filter (cut-off at 520 nm). The short-pass filter suppresses elastically scattered light and Stokes band fluorescence, which permits optical quantification of small thermal gradients.

Knowing the dyes' emission strength as a function of temperature, we mapped the thermal field around the near-IR laser focus (Fig. 5b). A NIR-absorbing dye was added to the aqueous medium in these experiments in order to increase the thermal gradient, so that it could be visualized with this optical technique. Therefore, the gradient measured in this experiment is significantly larger than in the previous experiment and could be used to rotate a larger droplet. Although the raw intensity data is affected by substantial pixel noise, radial averages around the laser's focal center provide a reasonable estimate of the temperature of the aqueous medium as a function of distance from the laser focus (Fig. 5c), which is well approximated with a simple power law (Supplementary section I.D). This allowed us to quantify the thermal differential that the droplets were experiencing as a function of distance to the laser for various values of laser currents. With this knowledge, we quantify the correlation between the temperature differential ΔT across a droplet and its steady state tilt (Fig. 5d-f), which we determined by side-view optical microscopy. The measured steady state rotation angle α^* is used to quantify the gravitational torque, which is equal in magnitude to the thermal torque (Fig. 5g). Theoretical predictions from our simple analytical model obtained by substituting the measured temperature profile in the equation of the thermal energy (eq. (2)) are in good quantitative agreement with the experimental observations for rotation angle and torque (Fig. 5f, g). The thermal differential needed to induce droplet rotation is smaller than 0.05 °C across the diameter of the droplet.

In summary, Janus emulsion droplets dynamically reorient in a thermal gradient. These rotations are due to thermocapillary effects occurring at the droplets' internal interface. A temperature gradient across the surfactant-free internal interface generates an interfacial tension differential that induces Marangoni-type fluid motion within the droplets, entraining flows around them. With the internal interface being the driver for the droplet reorientation, droplet morphology strongly influences the response to thermal gradients: Droplets with highly curved interfaces rotate more than those with a flatter internal capillary surface. Bi-phase emulsion droplets with a surfactant-free internal interface thus harbor a built-in motor that is activated via a temperature differential across the droplet. The rotational effect of thermocapillary motion in surfactant-stabilized multi-phase droplets

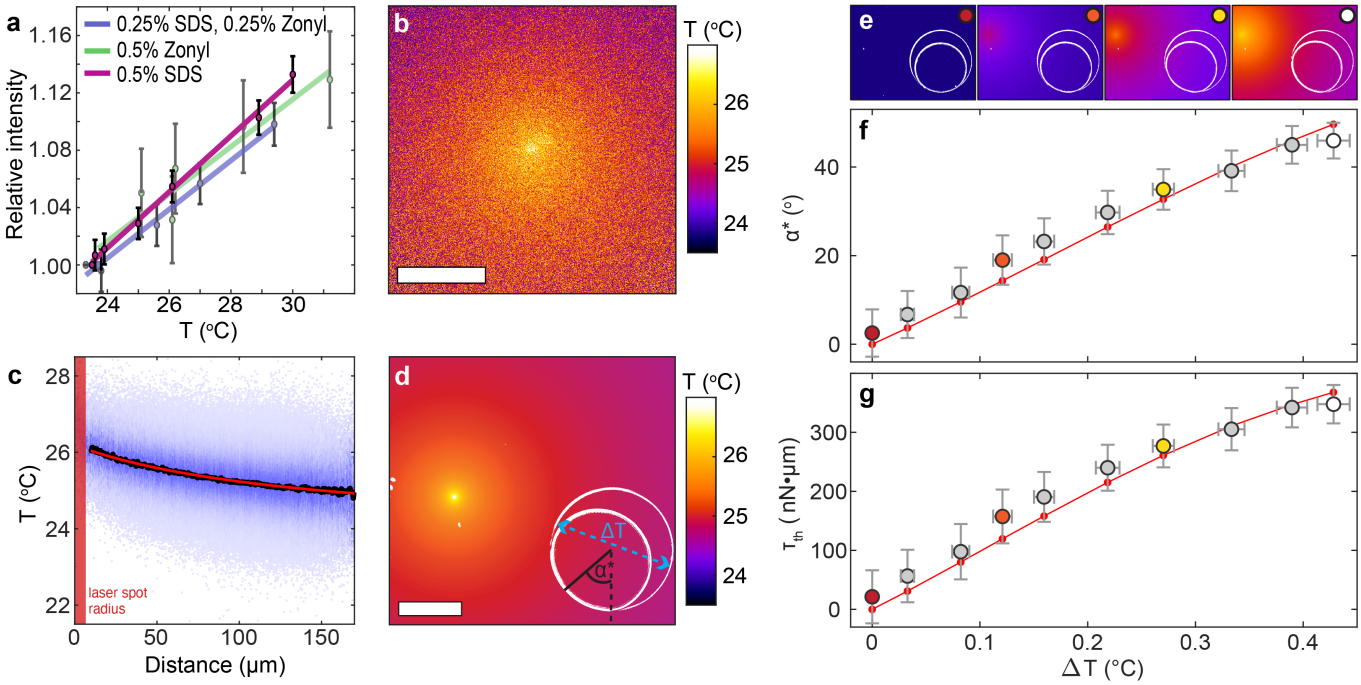

FIG. 5. **Quantifying droplet rotation and torque as a function of temperature differential.** **a)** Temperature dependence of emission intensity of Fluorescein 27 with different SDS and Zonyl surfactant concentrations in the aqueous medium relative to emission at room temperature. **b)** Temperature distribution around laser measured from the relative intensity of Fluorescein 27 using the fit shown in (a); scale bar: 100 μm. **c)** Measured temperature (blue) as a function of distance from the laser with mean values (black) and fit (red). **d)** Temperature map around laser spot using the fit shown in (c) with optical micrograph overlay of droplet; scale bar 100 μm. **e)** Optical micrograph overlays of fitted temperature distribution for laser currents of 0.5 A, 0.8 A, 1.1 A and 1.4 A. **f)** Rotation of droplet as a function of temperature differential ΔT across the droplet, as shown in (d). **g)** thermal torque τ_{th} vs. ΔT. Data points shown in color in (f, g) correspond to images in (e) marked with the same color. Experimental observations match the theoretically predicted behavior (red curves).

described here for the first time could prove important in micro-fluidic sorting, droplet mixing, micro-reactors, thermally controlled adaptive micro-optical systems, and opto-fluidic calorimetric sensors that translate micron-scale heat flows into optically detectable deflections of light.

I. ACKNOWLEDGMENTS

We thank Prof. Dr. Lauren Zarzar (Penn State University) for inspiring discussions at the start of this project. S.N. and M.K. acknowledge support by the National Science Foundation's CBET programme on "Particulate and Multiphase Processes" under grant number 1804241 and from the US Army Research Office through the Institute for Soldier Nanotechnologies at MIT under contract no. W911NF-13-D-0001. J.F.T. acknowledges support through a Feodor Lynen Fellowship of the Alexander von Humboldt Foundation. This research was supported in part by a Vannevar Bush Faculty Fellowship to T.M.S. (Grant # N000141812878).

[1] H.-D. Xi, H. Zheng, W. Guo, A. M. Gañán-Calvo, Y. Ai, C.-W. Tsao, J. Zhou, W. Li, Y. Huang, N.-T. Nguyen, and S. Hwa Tan, Lab Chip **17**, 751 (2017).
[2] L. Liu, N. Xiang, and Z. Ni, Electrophoresis **41**, 833 (2020).
[3] H. Zappe, *Fundamentals of Micro-Optics* (Cambridge University Press, 2010-09-30).
[4] T. Nisisako, Curr. Opin. Colloid Interface Sci. **25**, 1 (2016).
[5] L. D. Zarzar, V. Sresht, E. M. Sletten, J. A. Kalow, D. Blankschtein, and T. M. Swager, Nature **518**, 520 (2015).
[6] T. Sheth, S. Seshadri, T. Prileszky, and M. E. Helgeson, Nat Rev Mater **5**, 214 (2020).
[7] M. A. Augustin and Y. Hemar, Chem. Soc. Rev. **38**, 902 (2009).
[8] C.-X. Zhao, Adv. Drug Deliv. Rev. **65**, 1420 (2013).
[9] S. Nagelberg, L. D. Zarzar, N. Nicolas, K. Subramanian, J. A. Kalow, V. Sresht, D. Blankschtein, G. Barbastathis,

M. Kreysing, T. M. Swager, and M. Kolle, Nat. Commun. **8**, 14673 (2017).

[10] A. E. Goodling, S. Nagelberg, B. Kaehr, C. H. Meredith, S. I. Cheon, A. P. Saunders, M. Kolle, and L. D. Zarzar, Nature **566**, 523 (2019).

[11] A. E. Goodling, S. Nagelberg, M. Kolle, and L. D. Zarzar, ACS Mater. Lett. **2**, 754 (2020).

[12] T. M. Swager, Angew. Chem. Int. Ed. **57**, 4248 (2018).

[13] Q. Zhang, S. Savagatrup, P. Kaplonek, P. H. Seeberger, and T. M. Swager, ACS Cent. Sci. **3**, 309 (2017).

[14] L. D. Zarzar, J. A. Kalow, X. He, J. J. Walish, and T. M. Swager, Proc. Natl. Acad. Sci. U.S.A. **114**, 3821 (2017).

[15] L. Zeininger, S. Nagelberg, K. S. Harvey, S. Savagatrup, M. B. Herbert, K. Yoshinaga, J. A. Capobianco, M. Kolle, and T. M. Swager, ACS Cent. Sci. **5**, 789 (2019).

[16] V. B. Patravale and S. D. Mandawgade, Int. J. Cosmet. Sci. **30**, 19 (2008).

[17] S. H. Davis, Ann. Rev. Fluid Mech. **19**, 403 (1987).

[18] M. G. Velarde and R. K. Zeytounian, eds., *Interfacial Phenomena and the Marangoni Effect*, CISM International Centre for Mechanical Sciences, Vol. 428 (Springer Vienna, 2002).

[19] C. N. Baroud, in *Encyclopedia of Microfluidics and Nanofluidics*, edited by D. Li (Springer US, 2013) pp. 1–7.

[20] J. Thomson, Lond. Edinb. Dubl. Phil. Mag. **10**, 330 (1855).

[21] M. Schmitt and H. Stark, Phys. Fluids **28**, 012106 (2016).

[22] B. V. Hokmabad, K. A. Baldwin, C. Krüger, C. Bahr, and C. C. Maass, Phys. Rev. Lett. **123**, 178003 (2019).

[23] A. Diguet, R.-M. Guillermic, N. Magome, A. Saint-Jalmes, Y. Chen, K. Yoshikawa, and D. Baigl, Angew. Chem. **48**, 9281 (2009).

[24] P. Illien, R. Golestanian, and A. Sen, Chem. Soc. Rev. **46**, 5508 (2017).

[25] N. O. Young, J. S. Goldstein, and M. J. Block, J. Fluid Mech. **6**, 350 (1959).

[26] M. Muto, M. Yamamoto, and M. Motosuke, Anal. Sci. **32**, 49 (2016).

[27] B. J. Won, W. Lee, and S. Song, Sci. Rep. **7**, 3062 (2017).

[28] W. Hu and A. T. Ohta, Microfluid. Nanofluid. **11**, 307 (2011).

[29] C. N. Baroud, J.-P. Delville, F. Gallaire, and R. Wunenburger, Phys. Rev. E **75**, 046302 (2007).

[30] M. Robert de Saint Vincent, R. Wunenburger, and J.-P. Delville, Appl. Phys. Lett. **92**, 154105 (2008).

[31] D. S. Morton, R. S. Subramanian, and R. Balasubramaniam, Phys. Fluids A **2**, 2119 (1990).

[32] L. Rosenfeld, O. M. Lavrenteva, and A. Nir, J. Fluid Mech. **626**, 263 (2009).

[33] J.-C. Baret, Lab Chip **12**, 422 (2012).

[34] J. Chen and K. J. Stebe, J. Fluid Mech. **340**, 35 (1997).

[35] H. S. Kim and R. S. Subramanian, J. Colloid Interface Sci. **127**, 417 (1989).

[36] C. M. Leong, Y. Gai, and S. K. Y. Tang, Phys. Fluids **30**, 032002 (2018).

[37] E. Lauga and T. R. Powers, Rep. Prog. Phys. **72**, 096601 (2009).

[38] B. J. Park and D. Lee, ACS Nano **6**, 782 (2012).

[39] H. Rezvantalab and S. Shojaei-Zadeh, Soft Matter **9**, 3640 (2013).

[40] A. T. Oratis, T. P. Farmer, and J. C. Bird, Soft Matter **13**, 7556 (2017).

[41] C. E. Estrada-Pérez, Y. A. Hassan, and S. Tan, Rev. Sci. Instrum. **82**, 074901 (2011).

[42] J. A. Sutton, B. T. Fisher, and J. W. Fleming, Exp. Fluids **45**, 869 (2008).

[43] M. C. J. Coolen, R. N. Kieft, C. C. M. Rindt, and A. A. van Steenhoven, Exp. Fluids **27**, 420 (1999).

[44] See Supplemental Material (insert URL in proof) for details on experimental measurement procedures and a detailed theoretical derivations, which includes Refs. [45,46].

[45] J. Schindelin, I. Arganda-Carreras, E. Frise, V. Kaynig, M. Longair, T. Pietzsch, S. Preibisch, C. Rueden, S. Saalfeld, B. Schmid, J.-Y. Tinevez, D. J. White, V. Hartenstein, K. Eliceiri, P. Tomancak, and A. Cardona, Nat. Methods **9**, 676 (2012).

[46] B. McClain, M. Yoon, J. Litster, and S. Mochrie, Eur. Phys. J. B **10**, 45 (1999).